

NAVIER-STOKES COMPUTATIONS OF A COMPLETE HELICOPTER CONFIGURATION ACCOUNTING FOR MAIN AND TAIL ROTORS EFFECTS

T. Renaud, C. Benoît, J.-C. Boniface, P. Gardarein
Office National d'Etudes et de Recherches Aéropatiales,
BP 72, 92322 Châtillon Cedex, France

Abstract

The rotor-fuselage interaction is studied on the Dauphin 365N helicopter configuration. This research is carried out within the French-German cooperation CHANCE (Complete Helicopter Advanced Computational Environment). In the computations, the simulation of the main rotor and the fenestron is simplified by using a lifting surface model, called actuator disk, which represents the time-averaged loads of the rotor in a steady flow. Different models of forces distributions on the actuator disk are available. The fuselage pressure coefficients are in good agreement with experiment, with the non-uniform actuator disk hypothesis. On a complete helicopter with main and tail rotors, the Chimera method is used to model the main rotor. In climb flight conditions, the main rotor downwash interacts with the fenestron and modifies significantly the fenestron flow characteristics.

Notations

Re	Reynolds number, m^{-1}
V_∞	Freestream velocity, m/s
M_∞	Freestream mach number
α	Fuselage angle of incidence, degree
β	Fuselage sideslip angle, degree
P_i	Stagnation pressure, N/m^2
$P_{i\infty}$	Freestream stagnation pressure, N/m^2
K_p	Pressure coefficient
C_f	Friction coefficient
Y^+	Non-dimensional cell thickness
μ	Advance ratio
C_T	Rotor thrust coefficient
σ	Rotor solidity

$$\overline{T}_{Rotor} = \frac{100 T_{Rotor}}{\frac{1}{2} \rho (\omega R^2)_{Rotor} S_{Rotor} \sigma_{Rotor}}$$

Non-dimensional thrust of the rotor

$$SC_x = \frac{X}{0.5 \rho_\infty V_\infty^2}$$

Drag force coefficient in the aircraft reference frame

$$SC_y = \frac{Y}{0.5 \rho_\infty V_\infty^2}$$

Side force coefficient in the aircraft reference frame

$$SC_z = \frac{Z}{0.5 \rho_\infty V_\infty^2}$$

Lift force coefficient in the aircraft reference frame

$$SC_l = \frac{L}{0.5 \rho_\infty V_\infty^2}$$

Roll moment coefficient in the aircraft reference frame

$$SC_m = \frac{M}{0.5 \rho_\infty V_\infty^2}$$

Pitch moment coefficient in the aircraft reference frame

$$SC_n = \frac{N}{0.5 \rho_\infty V_\infty^2}$$

Yaw moment coefficient in the aircraft reference frame

Introduction

Due to the inherent complexity of the flowfield around helicopters, advanced tools have to be used in order to represent accurately the various phenomena, which occur on the helicopter. At low speed flight or in hover, the main rotor downwash impinges and interacts with the fuselage. The tail rotor and the fuselage also modify the main rotor inflow. Up to now, the design of a new rotorcraft has taken into account this complex interaction by experiments or simple methods. In fact, the use of CFD methods can significantly improve the design and solve eventual problems early in the program, which will be more efficient and less expensive. These CFD models of increasing accuracy have still to be validated by comparing numerical and experimental results.

Before numerical progress for rotor/fuselage interactions comprehension, the initial research was based on experiments. A classification of aerodynamic interactions was reviewed by Sheridan and Smith (Ref. 1). At NASA Langley, Berry and Althoff (Ref. 2) conducted experimental and numerical research on a main rotor and a simplified fuselage. In Europe, experimental investigations were also developed on various helicopter powered models (Ref. 6).

The first numerical attempts were realized with quasi-steady or unsteady panel methods coupled with prescribed wake or lifting line free wake. Thanks to the improvement of computers efficiency,

the next step thus naturally concerned viscous Navier-Stokes computations. An important progress to simulate rotor/fuselage interactions was achieved by Zori et al. (Ref. 3) and Chaffin et al. (Ref. 4) who used embedded body forces to model the time-averaged downwash produced by the rotating blades. In this quasi-steady representation of the rotor – called actuator disk, the thrust and the swirl velocities were modeled as a jump in pressure and in tangential velocities across the disk surface. Finally, it must be noticed that unsteady simulations representing the rotating blades have also been performed with Chimera technique. More recently, the viscous interactions of the main rotor with the fuselage for a realistic helicopter was computed in forward flight, using Vorticity Confinement (Ref. 5). At ONERA, the simulation of rotor/fuselage interactions has been studied for several years by various methods. First, the *PEIRF* code, based on a quasi-steady iterative coupling between two panel methods – one for the rotor and another one for the fuselage- has been developed and validated on realistic configurations (Ref. 6). Actuator disk models have been also used within Navier-Stokes *FLU3M* code and the new object-oriented *elsA* solver (Ref. 7, 8). Similarly, unsteady simulations with rotating blades have been studied in Euler mode (Ref. 9). The present studies are performed within the French-German cooperation CHANCE.

Numerical method

elsA solver

ONERA has started in 1996 the unification of his different aerodynamic solvers in a unique object-oriented code, *elsA* (Ensemble Logiciel de Simulation en Aérodynamique). It is based on multiblock structured meshes where Reynolds averaged Navier-Stokes equations in a finite volume formulation allow to simulate a large variety of applied configurations (aircraft, turbomachinery, helicopters, ...).

For the present computations, the 2nd order discretization in space Jameson scheme with a scalar artificial viscosity has been used with Martinelli's correction. The time integration can be resolved either by an implicit residual smoothing phase with a 4th order Runge-Kutta technique or by an implicit LU scalar relaxation phase associated to a backward Euler scheme. Multigrid approach allows to accelerate the convergence. In order to avoid poor results in terms of convergence rate and solution accuracy in low subsonic flow regime, local preconditioning method is used with Merkle and Choi technique (Ref. 10). The *elsA* solver contains numerous turbulence models and for all the turbulent Navier-Stokes results of this paper, the two-equation Smith k-l model was used. For the present

helicopters configurations, adiabatic wall condition is applied on the fuselage.

Actuator disk model

The simulation of a rotating machine (propeller, rotor, ...) can be simplified by modeling the rotor with a lifting surface, called "actuator disk". It represents the time-averaged loads of the rotor in a steady flow computation. Due to the steady-state assumption, a large reduction of computational cost is achieved by comparison with an unsteady computation of the flow around rotating blades. A bibliography and a description of the different numerical techniques to integrate an actuator disk can be found in Ref. 11. Two numerical implementations of the model are available in *elsA*: the boundary condition can be treated either as an inlet/outlet condition or as a matching condition with a source term. The first one uses a characteristic formulation for which the fluxes are upgraded with the actuator disk terms. The second formulation, used in the present computations, behaves like an usual interface and the actuator disk source terms are simply added to residuals for the cells lying underneath the lifting surface.

The source terms, which model the discontinuities of the flowfield, are calculated by a uniform momentum equilibrium with the global lift (Fig. 1) or by using a lifting line method to provide the momentum variations in the radial and azimuthal directions on the disk (non-uniform actuator disk). In the present study and for non-uniform actuator disk, the aerodynamic loads of the rotor come from a rotor trim computed with the Eurocopter *HOST* software. The *HOST* code uses lifting lines theory to provide local forces on one rotor blade in the blade reference frame. An interface between *HOST* and *elsA* allows to compute the aerodynamic force distribution on the actuator disk.

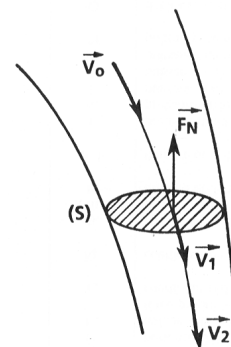


Fig. 1 – Representation of the flow downwash through an actuator disk with a global lift \vec{F}_N

Chimera technique

The Chimera method allows to simplify the process of mesh generation by using overlapping grids. The Chimera technique enables transfers between grids, first at overlapping boundaries, then around blanked

areas corresponding to solid bodies, actuator disk, ... The transfers are carried out by interpolation on conservative variables. In the *elsA* software, several methods and parameters are available (Ref. 12): the cell search procedure like the ICG method (interpolation cartesian grid) for unsteady flows or the ADT method (alternating digital tree) for steady flows, the shape used for blanking (cartesian, cylindrical, ...). For the present computations, the ADT method has been used.

S2Ch Dauphin 365N configuration

The method has been applied on different helicopter configurations.

As a first test case, one considers the Dauphin 365N helicopter model in the following flow conditions: freestream velocity $V_\infty=15\text{m/s}$ ($M_\infty=0.044$), Reynolds number $Re=1.07 \cdot 10^6 \text{ m}^{-1}$ and angle of incidence $\alpha=-3^\circ$. This scale 1/7.7 powered model has been intensively tested in the S2Ch wind tunnel during the 90's. The main characteristics of the Dauphin powered model are the following:

- Rotor radius $R=0.75\text{m}$
- Blade root cutout $R_{\text{cut}}=0.206\text{m}$
- Blade chord $c=0.05\text{m}$
- Rotor solidity $\sigma=0.0849$
- Blade tip velocity $\Omega R=100\text{m/s}$
- Fuselage length $L_{\text{fuselage}}=1.5\text{m}$
- No fenestron

Aerodynamic variables for those conditions are:

- $\mu=0.15$
- $C_T/\sigma=0.0725$; $\overline{T}_{\text{main rotor}}=14.5$
- $\rho_\infty=1.225 \text{ kg/m}^3$; $T_\infty=288.15 \text{ K}$; $p_\infty=101325 \text{ Pa}$

Figure 2 shows the aerodynamic lift force distribution on the non-uniform actuator disk.

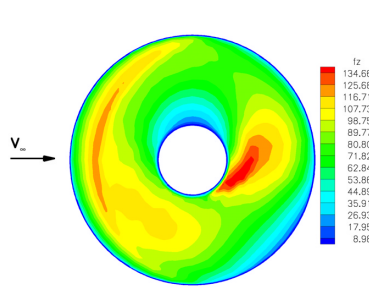


Figure 2 - Aerodynamic lift force component F_Z of the non-uniform actuator disk for the Dauphin 365N

The mesh has been constructed at ONERA with the *ICEM-CFD* software (Ref. 9). The CAD geometry has been simplified (fenestron removed, simplification of the engines fairing geometry, no modelization of the strut and of the rotor hub). The Navier-Stokes grid takes into account the actuator disk mesh. The finest grid has a total of about 7 millions points distributed in 97 blocks. The coarse grid has been obtained by taking one another point in all directions and has a total of about 1 million points. Figure 3 shows a general view of the fine grid, specifying the fuselage and the rotor surface.

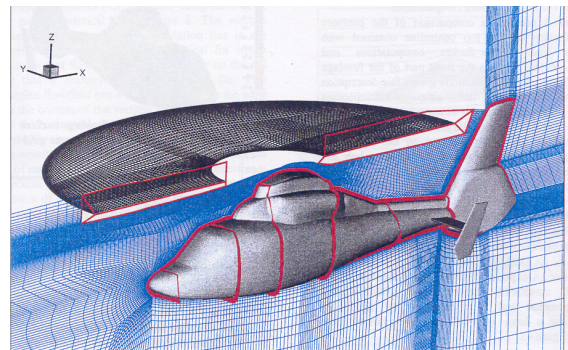


Fig. 3 – General view of the fine Navier-Stokes grid around the Dauphin 365N fuselage and its rotor surface

Coarse grid results

Computations of the isolated fuselage without the main rotor, of the fuselage with uniform actuator disk and of the fuselage with non-uniform actuator disk have been performed first on the coarse grid. These flow solutions have been converged decreasing the low speed preconditioning parameter (i.e. strong preconditioning).

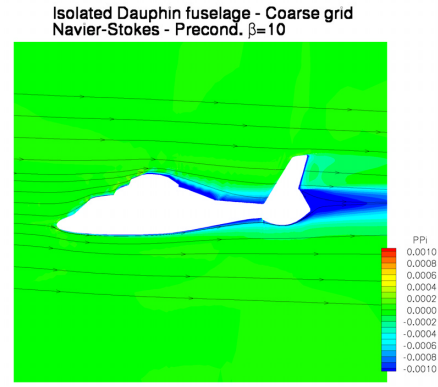
Final results of aerodynamic loads and moments coefficients are given in table 1. One particularly notices the influence of the actuator disk model on the lift coefficient: this coefficient has been increased with respect to the isolated fuselage solution, due to the impact of the rotor downwash on the helicopter. Adversely, there is only little influence on the drag coefficient between the isolated fuselage and the fuselage with actuator disk configurations. The non-uniform model of the actuator disk condition involves the largest effect on the roll moment coefficient, as this configuration introduces a dissymmetry in the flow.

Table 1 – Aerodynamic forces and moments coefficients for coarse grid computations

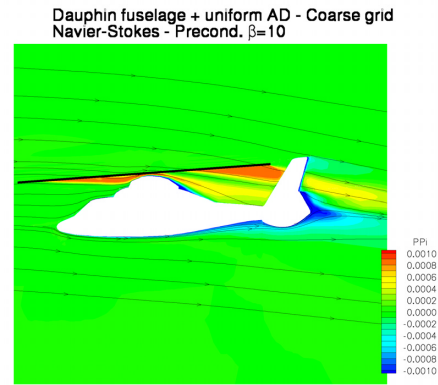
	Isolated fuselage	Uniform actuator disk	Non-uniform actuator
SC_x	0.014	0.014	0.0153
SC_y	-0.0138	-0.018	-0.02
SC_z	-0.0137	-0.0354	-0.0288
SC_l	0.0027	0.0011	0.0024
SC_m	0.0017	0.0174	0.01
SC_n	-0.0081	-0.0158	-0.0263

The figure 4 shows the isocontours of stagnation pressure rate $PP_i = \frac{P_i - P_{i\infty}}{P_{i\infty}}$ on the isolated fuselage

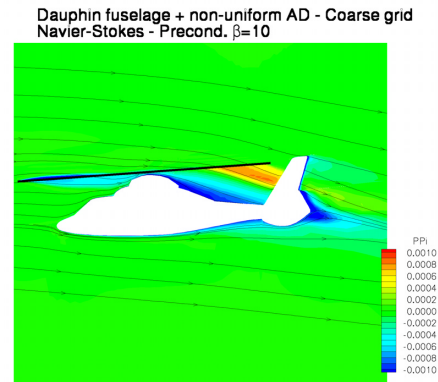
and for rotor/fuselage interaction (uniform or non-uniform actuator disk). Without the main rotor, the stagnation pressure is decreased, behind the engine fairing corresponding to the flow separation region; there is also a separated flow region behind the tail. When the main rotor is accounted for, the rotor downwash deflects the flow streamlines with an increase of stagnation pressure downstream of the rotor. In this figure 4, only few differences are seen between the effect of an uniform and a non-uniform actuator disk: with a uniform load, the stagnation pressure increment at the front part of the rotor interacts with the fuselage near the engine fairing and reduces the depression zone due to the separation. At the rear part of the rotor, the stagnation pressure increment impacts on the tail and reduces the wake of the fuselage. With a non-uniform actuator disk, the stagnation pressure increment at the front part of the rotor is replaced by a loss of stagnation pressure, which tends to increase the separation zone behind the engine fairing. One can observe that the streamlines at the front part of the rotor are deviated upwards before being “sucked” down by the actuator disk. The stagnation pressure increment in the wake of the rotor seems to be weaker for the non-uniform actuator disk configuration than in the configuration with a uniform actuator disk (figure 4b and 4c).



(a)



(b)



(c)

Figure 4 – Isocontours of $PP_i = \frac{P_i - P_{i\infty}}{P_{i\infty}}$ for : (a) isolated fuselage (b) fuselage with uniform actuator disk (c) fuselage with non-uniform actuator disk

This qualitative description of the flow allows to better understand the repartition of pressure coefficient on the fuselage (figure 5). The flow deflected by the rotor downwash impacts more strongly on the fuselage, in particular on the nose, the tail boom and the tail. With a non-uniform actuator disk, the pressure coefficient K_p values decrease on the tail boom as the separation area is more important than with an uniform actuator disk.

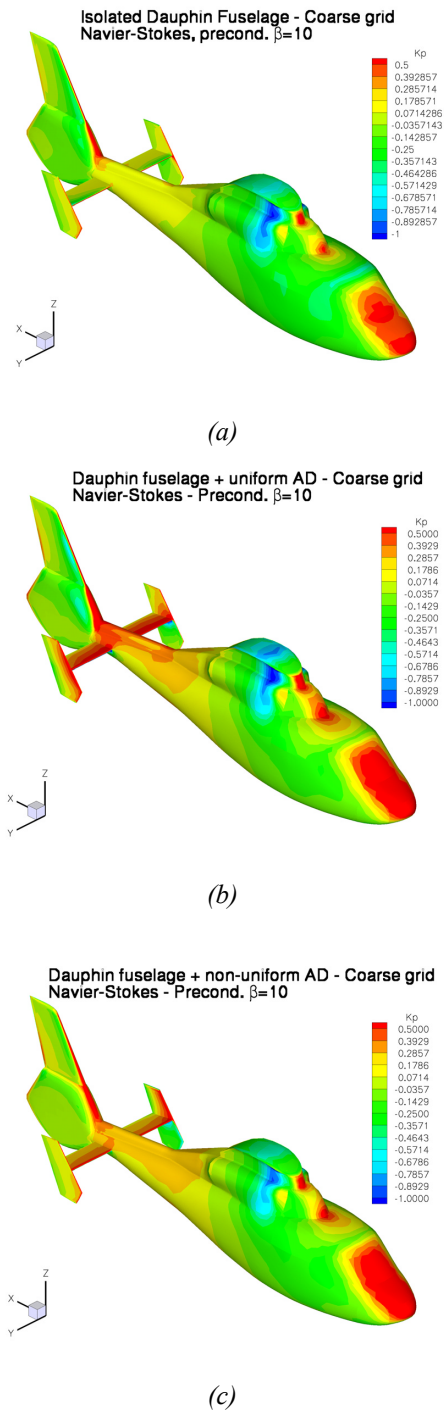


Figure 5 – Isocontours of pressure coefficient for: (a) isolated fuselage (b) fuselage with uniform actuator disk (c) fuselage with non-uniform actuator disk

The figure 6 presents a comparison along the helicopter centerline of computed pressure coefficient K_p with experiment. On the bottom centerline, one notices that the strut, which is not accounted for in the computations, has a significant influence in the zone $0.3 < x < 0.8$. In general, improvement of the numerical results is noted when the actuator disk is activated (for instance, at the

front part of the fuselage along the top and bottom centerlines). On the top centerline, with an uniform actuator disk, the pressure coefficient is overestimated on the tail boom. The results with a non-uniform model are in good agreement with the experiment. It remains a gap between the computed and the experimental values in the separation area behind the engine fairing ($0.6 < x < 0.9$); the coarse grid can be a reason for this difference. The figure 7 shows the evolution of the friction modulus coefficient on lower and upper centerlines. We note again two separation areas, on the lower centerline under the tail at $x=1.2$ and behind the engine fairing on the upper centerline at $x=0.8$. The configuration with non-uniform actuator disk presents the weakest separation on the engine fairing.

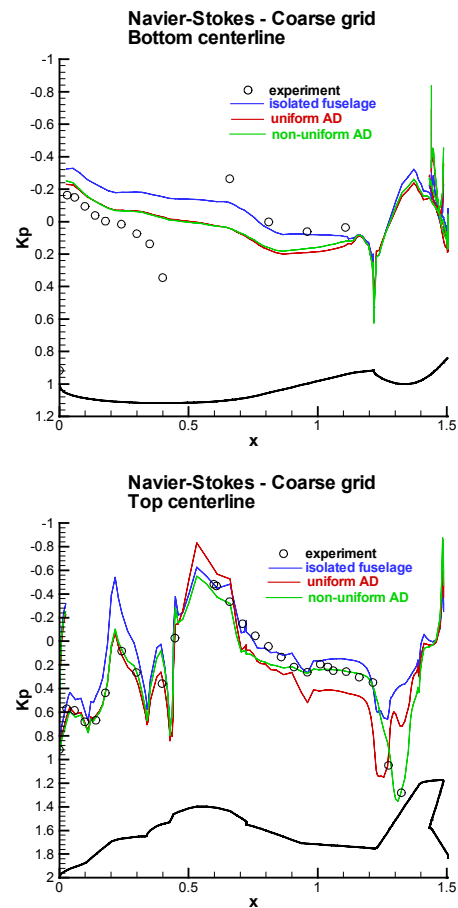


Figure 6 – Effect of actuator disk – Pressure coefficient along centerlines

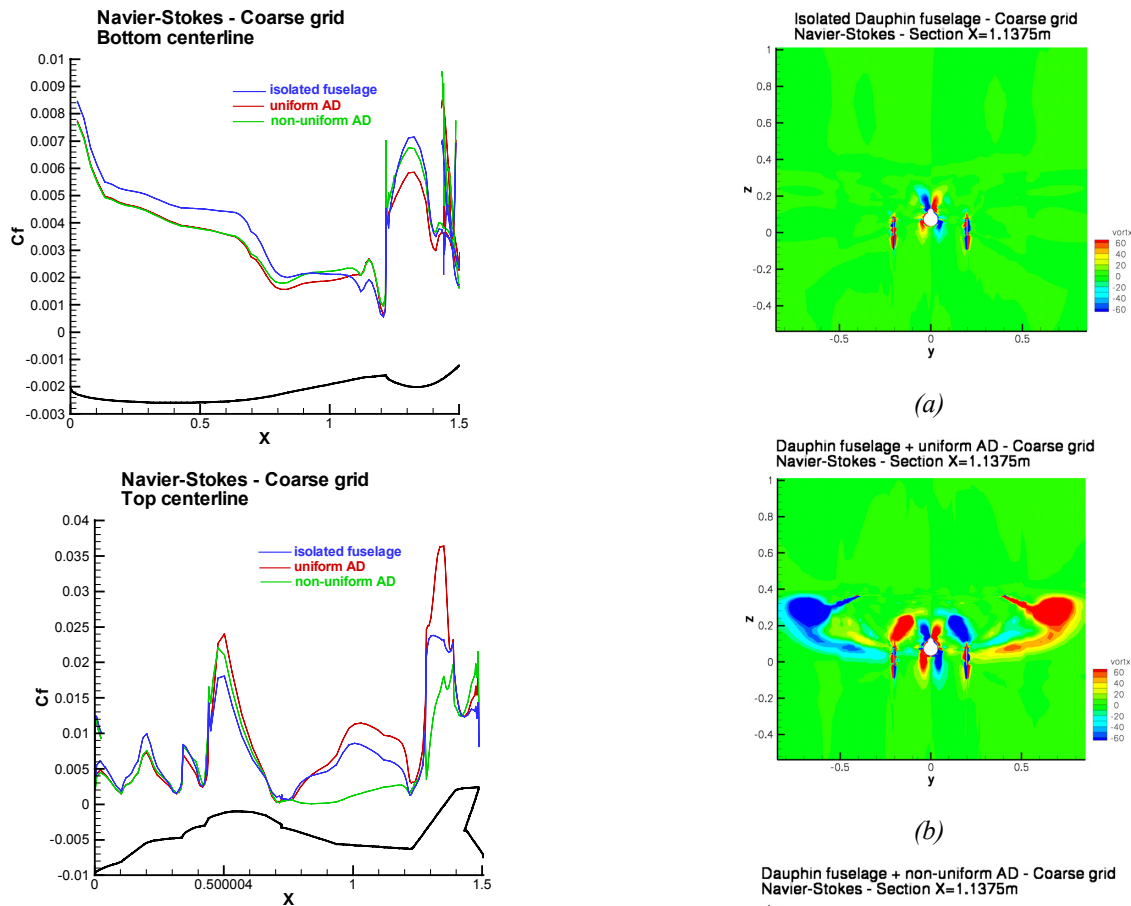


Figure 7 – Effect of actuator disk – Friction coefficient along centerlines

The rotor downwash may be identified by the strong vorticity areas in the downstream regions. The vorticity contours are analysed on the figure 8 for a section crossing the tail boom (x-component of the vorticity). Without the main rotor (isolated fuselage case on fig. 8a), the flow vorticity is confined close to the fuselage geometry. When the rotor is modelled, large vorticity zones appear at the rotor extremities, corresponding to two contra-rotating vortices (fig. 8b and 8c). The same observation is valid for the vortex due to the central hole of the actuator disk in both computations. We can note the effect of the rotor downwash, which enlarges the two vorticity areas under the tail boom. A dissymmetry appears in the figure with a non-uniform actuator disk (fig. 8c). For the present rotor which rotation is clockwise, we can note that the counterclockwise vorticity zone near the left empennage (advancing blade) increases whereas the clockwise vorticity zone near the right empennage (retreating blade) disappears with respect to the uniform actuator disk configuration. The vorticity results for non-uniform actuator disk (fig. 8c) is in rather good agreement with the experimental results provided on figure 8d.

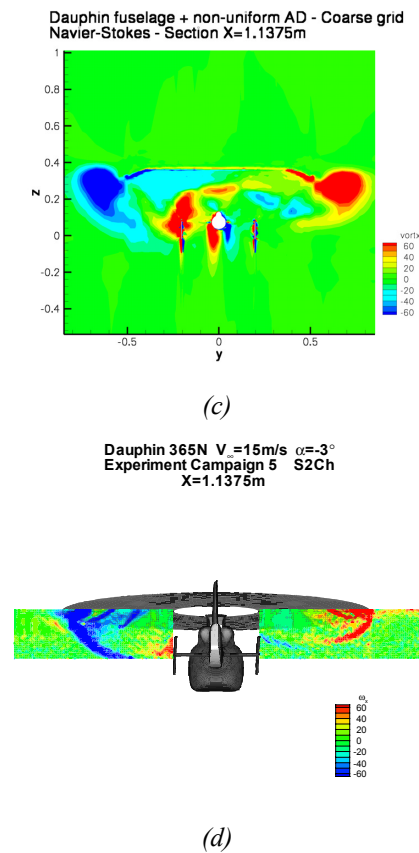


Figure 8 – Isocontours of x-component of vorticity for : (a) isolated fuselage (b) fuselage with uniform actuator disk (c) fuselage with non-uniform actuator disk (d) fuselage with rotor during S2Ch experiment

Fine grid results

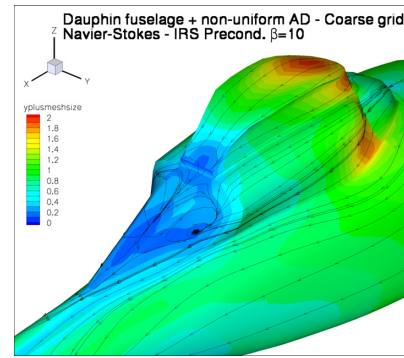
In this part, we analyse the grid density influence on the interaction between the Dauphin fuselage and a non-uniform actuator disk; the previous results obtained on a medium mesh (1 Million points) are compared with results obtained with a fine grid (about 7 Millions points). The pressure coefficients on the fuselage are modified only slightly by the mesh refinement.

Table 2 summarises the numerical (coarse and fine grids) results for the aerodynamic forces and moments coefficients: the mesh refinement influences principally the SC_x (drag force coefficient). This can be interpreted as the result of a better simulation of the flow separation zone along the tail boom.

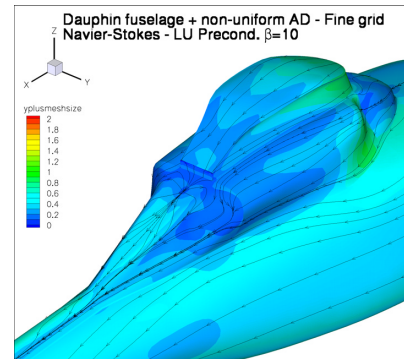
Table 2 – Aerodynamic forces and moments coefficients for fuselage computations with non-uniform actuator disk

	Coarse grid	Fine grid
SC_x	0.0153	0.0109
SC_y	-0.02	-0.0197
SC_z	-0.0288	-0.0317
SC_l	0.0024	0.0015
SC_m	0.01	0.0097
SC_n	-0.0263	-0.0249

On the figure 9, the friction is described as isocontours of Y^+ and streamlines are plotted on the fuselage surface. We focus the analysis on the area around the engine fairing. The Y^+ level decreases naturally with the mesh refinement. The mapping of the streamlines is influenced by the mesh refinement behind the engine fairing. The junction point of streamtraces is located higher with the fine grid and there is no more recirculation of the streamlines. The influence of the mesh refinement is more visible on friction coefficient on figure 10. The fine and coarse grid curves along the centerline differ from the engine fairing, in particular in the separation areas where the fine grid results show a larger separated flow region than the coarse grid results.



(a)



(b)

Figure 9 – Isocontours of Y^+ and streamlines - Navier-Stokes coarse/fine grid comparison

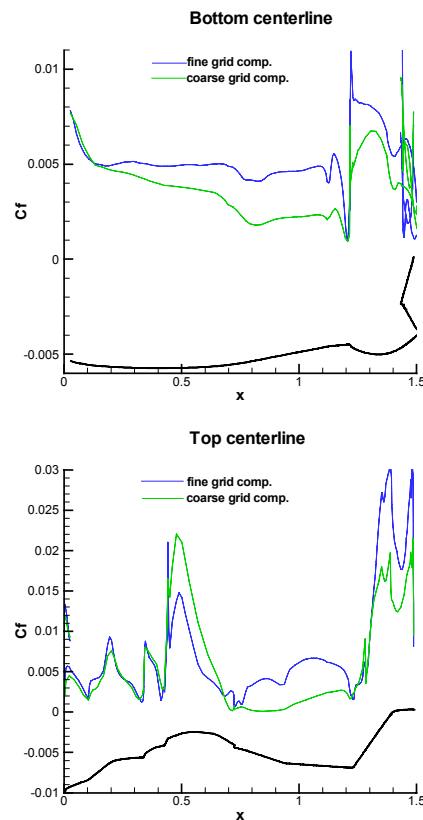


Figure 10 - Friction coefficient along fuselage centerlines – Navier-Stokes coarse/fine grid comparison

On the figure 11, the comparison of x-component of vorticity (in a x-section crossing the tail boom and the empennages) shows that the fine grid results present finer structures, for instance above the tail boom. The numerical solutions are in good agreement with the experimental results (cf. figure 8d).

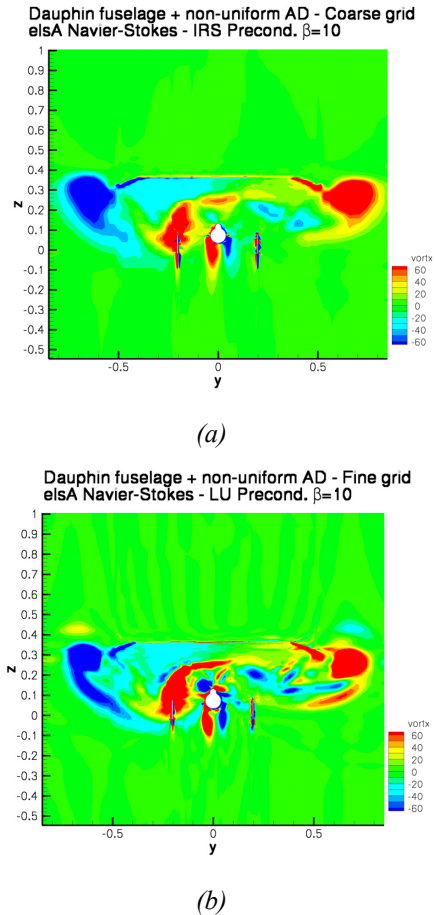


Figure 11 - Isocontours of x-component of vorticity – Navier-Stokes coarse/fine grid comparison

Dauphin 365N and fenestron configuration

The next step in the simulation of the complete helicopter is the interaction between the fuselage and both the main and tail rotors modelled by the actuator disk formulation. This part deals with computations of the flowfield around a simplified Dauphin configuration with its main rotor and its fenestron: the empennages are removed and the top of the engine fairing is simplified. The mesh of this scale 1 configuration is made of two grids as presented on figure 12: the background grid includes the fuselage and the fenestron area; an overlapped grid models the main rotor by an actuator disk thanks to the Chimera method implemented in *elsA*. The background grid, realised with *ICEM CFD Hexa*, contains about 5.4 Millions cells in 72 blocks. The computations are made in climb flight

conditions ($M_\infty=0.1136$, $\alpha=-11.9^\circ$, $\beta=-0.9^\circ$) and the influence of the main rotor modelization is analysed. Both the main rotor and the fenestron effects are simulated by an uniform actuator disk condition:

$$\overline{T}_{main\ rotor} = 14.25 \text{ and } \overline{T}_{fenestron} = 3.$$

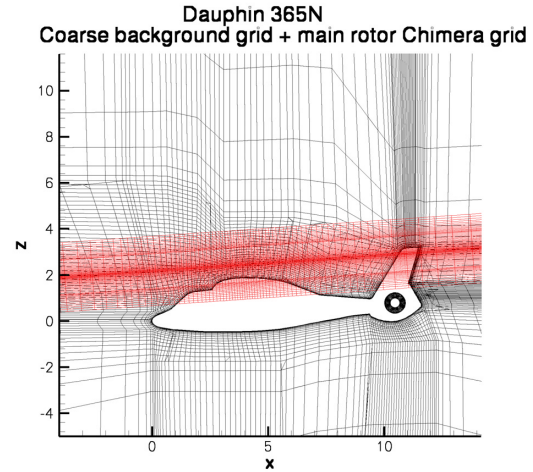


Figure 12 – Mesh of a simplified Dauphin configuration with its main rotor and its fenestron

These Navier-Stokes computations have been performed with a k-l turbulence model on the coarse grid (670000 cells) and the fine grid. The table 3 presents the drag, side and lift forces coefficients on the coarse and fine grids without and with the main rotor simulation. It can be noticed that the mesh refinement has an important effect on the loads results: the drag and side forces coefficients decrease with the finer grid, whereas the lift coefficient is increased. The effect of the main rotor simulation is also significant: the drag is increased due to the stronger wake induced by the actuator disk; the side force coefficient doesn't change a lot because the actuator disk condition is uniform in those computations; finally, the lift coefficient becomes more negative due to the impact of the rotor downwash on the fuselage.

Table 3 – Drag, side and lift forces coefficients with and without main rotor on the coarse and fine grids

	SC_x	SC_y	SC_z
Coarse grid without main rotor	1.66	-0.84	-1.15
Coarse grid with main rotor	2.31	-0.49	-2.67
Fine grid without main rotor	1.31	-1.13	-0.85
Fine grid with main rotor	1.76	-1.04	-1.85

The three-dimensional visualizations in figure 13 show the pressure coefficient repartition on the fuselage and the streamlines deviation into the fenestron. In such flight conditions, a recirculation area appears in the upstream part of the fenestron. On figure 14, the isocontours of the stagnation pressure variation $\frac{P_i - P_{i\infty}}{P_{i\infty}}$ show the effect of the main rotor on the flowfield. The rotor downwash, where the stagnation pressure variation is high, interacts directly with the fenestron in such climb flight conditions.

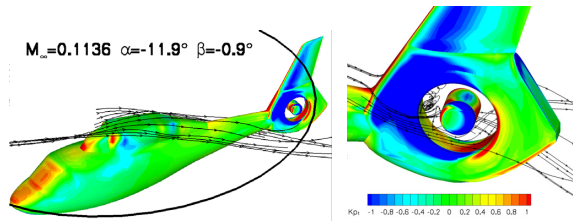


Figure 13 – Dauphin 365N + Fenestron (coarse grid) – Pressure coefficient on fuselage

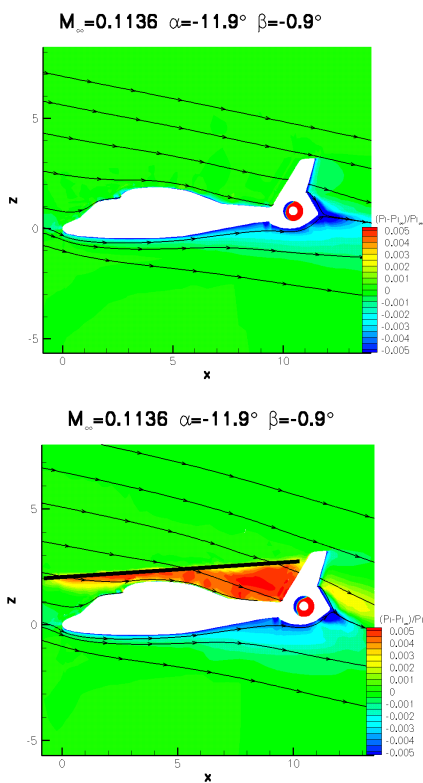


Figure 14 – Dauphin 365N + Fenestron (coarse grid) – Effect of the main rotor on the stagnation pressure variation

Figure 15 represents the isocontours of stagnation pressure ratio $\frac{P_i}{P_{i\infty}}$ into the fenestron on a horizontal median plane

slice. A comparison is made between the fine grid solutions with and without the main rotor. Upstream, the flow is sucked up by the fenestron. The flowfield is similar for both computations into the fenestron: in the front part ($10 < x < 10.25$), there is a recirculation area; in the rear part ($10.7 < x < 10.95$), the stagnation pressure ratio increases through the actuator disk condition. Downstream the fenestron channel, a little part of the flow is sucked up into the fenestron ($x \approx 10$). The streamlines below the fenestron are more deviated when the main rotor is activated. Thus, the recirculation area along the rear part of the fenestron ($x > 11$) becomes more developed. Figure 16 shows the same comparison for a vertical plane into the fenestron. The principal effect of the main rotor simulation deals with the recirculation area in the upper part of the fenestron ($z \approx 1.2$). When the main rotor flow is taken into account, the recirculation is more developed with two counter-rotative vortices due to the flow deviation towards the fenestron by the main rotor downwash. The separation point is changed which let the recirculation move through the actuator disk condition.

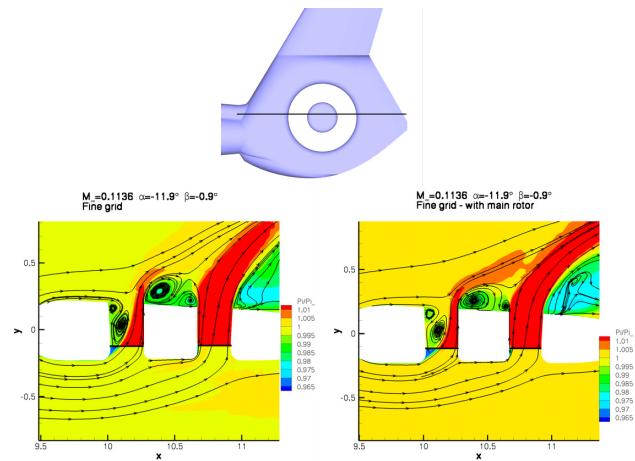


Figure 15 – Isocontours of stagnation pressure ratio on a horizontal median plane (fine grid)

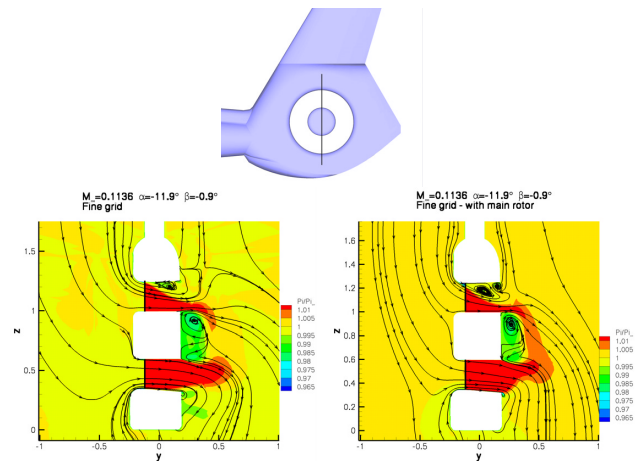


Figure 16 – Isocontours of stagnation pressure ratio on a vertical median plane (fine grid)

Conclusions

Within the French-German cooperation CHANCE, ONERA has performed rotor/fuselage interaction computations around a Dauphin 365N geometry in a quasi-steady assumption. The computations were performed for low speed forward flight ($V_\infty=15\text{m/s}$) with both uniform and non-uniform actuator disk conditions. Comparison of the numerical results with the experimental results of the powered model tested in the ONERA S2Ch wind tunnel shows that the rotor/fuselage interaction is better described with the non-uniform actuator disk modelization.

The mesh refinement analysis shows that a fine grid (7 Millions points) modifies only slightly the pressure coefficient distributions in the non-separated flow regions but modifies more significantly the friction coefficient levels. The mesh refinement allows also to predict more accurately the vorticity distributions by comparison with the experimental flowfield.

For the account of main and tail rotors, the Chimera technique proves to be very efficient. In climb flight, the influence of the main rotor downwash is significant on the flow characteristics in the vicinity of the fenestron.

The further studies of CHANCE on the complete helicopter simulation will concern the unsteady computation of the rotor and its interaction with the fuselage.

Acknowledgements

The authors would like to acknowledge the French Ministry of Transport (DPAC) and SPAé for the financial support of the numerical studies presented in this paper.

The authors are thankful towards Eurocopter for the Dauphin 365N data.

References

- [1] P. Sheridan, R. Smith
Interactional aerodynamics – A new challenge to helicopter technology
35th Annual Forum of the American Helicopter Society, Washington D.C., May 1979
- [2] J. D. Berry, S. L. Althoff
Inflow velocity perturbations due to the fuselage effects in the presence of a fully interactive wake
46th Annual Forum of the American Helicopter Society, Washington D.C., May 1990
- [3] L. A. J. Zori, S. R. Mathur, R. G. Rajagopalan
Three-dimensional calculations of rotor-airframe interaction in forward flight
48th Annual Forum of the American Helicopter Society, Washington D.C., June 1992
- [4] M. Chaffin, J. Berry
Navier-Stokes simulation of a rotor using a distributed pressure disk method
51st Annual Forum of the American Helicopter Society, Foth Worth, TX, May 1995
- [5] C. M. Wang, J. O. Bridgeman, J. S. Steinhoff, Y. Wenren
The application of computational vorticity confinement to helicopter rotor and body flows
49th Annual Forum of the American Helicopter Society, Washington D.C., May 1998
- [6] D. Gasser, N. Bettschart, B. Drouin
Theoretical and experimental studies on unsteady helicopter rotor-fuselage interactional aerodynamics
American Helicopter Society, Vertical Lift Aircraft Design Conference, San Francisco, CA, January 1995
- [7] N. Bettschart
Rotor-fuselage interaction: Euler and Navier-Stokes computations with an actuator disk
55th Annual Forum of the American Helicopter Society, Montreal, Canada, May 1999
- [8] J. Brezillon
Simulation of rotor-fuselage interactions by using an actuator disk
26th European Rotorcraft Forum, The Hague, Netherlands, September 2000
- [9] J. C. Boniface, P. Guillen, M. C. Le Pape, D. Darracq, P. Beaumier
Development of a Chimera unsteady method for the numerical simulation of rotorcraft flowfields
36th Aerospace Sciences Meeting & Exhibit, Reno, NV, January 1998
- [10] Y. H. Choi, C. L. Merkle
The application of preconditioning to viscous flows
Journal of Computational Physics, 105, pp. 207-233, 1993
- [11] F. Le Chuiton
Actuator disk modeling for helicopter rotors
28th European Rotorcraft Forum, Bristol, UK, September 2002
- [12] C. Benoît, M.-C. Le Pape, G. Jeanfaivre
Improvement of the robustness of the Chimera method
32nd AIAA Fluid Dynamics Conference & Exhibit, Saint-Louis, USA, June 2002